A 3-D Hybrid SEM-FK Method for Teleseismic Wave Simulation in Coupled Elastic-Acoustic Media

Nanqiao Du[*1], Sirawich Pipatprathanporn[3], Mijian Xu[2], and Qinya Liu[1,2]

Abstract

We present a three-dimensional hybrid numerical scheme developed for modeling teleseismic plane-wave propagation through coupled acoustic–elastic media. This approach integrates the 3-D spectral-element method (SEM) with a matrix-based frequency–wavenumber (FK) method, enabling the rigorous treatment of complex bathymetry and precise elastic–acoustic coupling within layered media. To facilitate large-scale simulations, the computational framework is optimized via GPU acceleration. The accuracy of the hybrid SEM–FK method is validated through a benchmark comparison with semi-analytical FK solutions for one-dimensional velocity structures. We demonstrate the practical utility of the method using a synthetic two-layer subduction zone model; specifically, we simulate receiver functions for ocean-bottom seismometers and perform a full-waveform inversion that successfully recovers prescribed subsurface anomalies. This hybrid SEM–FK framework provides an efficient and robust tool for receiver function analysis and scattering imaging, offering a powerful tool to investigate Earth's deep structure beneath oceanic regions.

Cite this article as Du et al. (2022). A 3-D Hybrid SEM-FK Method for Teleseismic Wave Simulation in Coupled Elastic-Acoustic Media, *Seismol. Res. Lett.* **XX**, 1–20, doi: 00.0000/000000000.

Supplemental Material

---

1. Department of Earth Sciences, University of Toronto, Toronto, Canada, https:// orcid.org/0000-0003-3623-7686 (FA); 2. Department of Physics, University of Toronto, Toronto, Canada, https://orcid.org/0000-0000-0000-0003 (SA); 3. Department of Geosciences, Princeton University, Princeton, NJ 08544, USA, https://orcid.org/0000-0000-0000-0003 (TA)

*Corresponding author: nanqiao.du@mail.utoronto.ca

Introduction

Unequal geographical data coverage remains a fundamental limitation in the seismic exploration of the Earth's interior, particularly in oceanic regions which encompass nearly 75% of the Earth's surface (Simon et al., 2021). Historically, this observational gap has been attributed to significant challenges regarding accessibility, operational costs, and technical limitations (Hammond et al., 2019; Rowe et al., 2022). However, recent technological advancements are beginning to bridge this divide.

In oceanic environments, specialized instrumentation is essential for high-quality data acquisition. Current state-of-the-art technologies include ocean-bottom seismometers (OBS) (Webb and Crawford, 2010; Arai et al., 2016; Wei et al., 2021; Yamaya et al., 2021), distributed acoustic sensing (DAS) systems (Zhan, 2020; Williams et al., 2021; Lin et al., 2024), and Mobile Earthquake Recording in Marine Areas by Independent Divers (MERMAID) (Simon et al., 2021; Pipatprathanporn and Simons, 2022). Each of these platforms requires specialized data processing workflows to effectively extract valuable signals, such as first-arrival P-waves (Nolet et al., 2024), surface waves, ambient noise (Luo et al., 2020), and receiver functions (RFs) (Yang et al., 2023). The integration of these methodologies signifies a promising evolution in our ability to characterize the complex seismic behavior of the oceans, contributing to more comprehensive global subsurface models.

Beyond traditional ray-based methods—which rely on simplified layered models and utilize only a small portion of the seismogram—finite-frequency waveform analysis and full-waveform inversion (FWI) (Tromp et al., 2005; Chen et al., 2007; Zhu et al., 2015) have gained significant prominence. These methods enhance imaging accuracy by leveraging the full physics of wave propagation to resolve intricate structures. However, accurate simulation in oceanic environments poses unique challenges, requiring the rigorous treatment of 3-D elastic–acoustic coupling at the seafloor. This interface often involves complex topographic variations that significantly affect high-frequency wavefields (Fernando et al., 2020; Wehner et al., 2022).

An additional complexity arises from teleseismic signals, where the seismic source is located at great distances from the receiver ($\Delta \geq 30°$). Precise simulation in such cases necessitates modeling within a 3-D global context (Komatitsch et al., 2000). To maintain computational efficiency, hybrid methods have been developed to couple results from low-complexity regions—typically represented by 1-D background models with semi-analytical solutions—with high-complexity regions where 3-D numerical methods are required (Liu et al., 2025). Existing hybrid frameworks utilize techniques such as the frequency–wavenumber (FK) method (Tong et al., 2017; Wang et al., 2022), the axisymmetric spectral-element method (AxiSEM) (Nissen-Meyer et al., 2008; Kan et al., 2023), mirror forces (Lyu et al., 2020), and transfer functions (Pipatprathanporn and Simons, 2024).

In this paper, we propose a novel hybrid method for computing the plane-wave injection response in oceanic environments. By integrating an FK method that accommodates fluid layers with the spectral-element method (SEM) (Komatitsch and Tromp, 1999), our approach effectively simulates teleseismic signals while capturing the inherent complexities of oceanic settings, such as bathymetry and water-layer reverberations. Furthermore, we derive waveform sensitivity kernels in both the elastic and acoustic domains, providing the theoretical basis for oceanic FWI. We validate the accuracy and efficiency of our method through two comprehensive numerical experiments, demonstrating its potential for enhancing seismic imaging and monitoring beneath the seafloor.

Methodology

The propagation of teleseismic waves satisfies the source-free wave equations (Aki and Richards, 2002):

$$\begin{aligned} &\rho \ddot{u}_i = \sigma_{ij,j} \\ &\sigma_{ij} = \lambda u_{k,k}\delta_{ij} + \mu(u_{i,j} + u_{j,i}) \end{aligned} \tag{1}$$

where ρ is the density, $u_i(\boldsymbol{x}, t)$ is the displacement, and σ_{ij} is the stress tensor, $u_{i,j} = \partial u_i / \partial x_j$, λ and μ are Lamé parameters for isotropic media. Throughout this paper, the Einstein summation convention is assumed unless otherwise stated. At acoustic–elastic interfaces, the following boundary conditions must be satisfied:

$$\begin{aligned} &[\mathbf{n}\cdot\boldsymbol{\sigma}\cdot\mathbf{n}]_-^+ = 0, \quad \text{(Continuity of normal traction)} \\ &[\mathbf{n}\cdot\mathbf{u}]_-^+ = 0, \quad \text{(Continuity of normal displacement)} \\ &[\mathbf{t}\cdot\boldsymbol{\sigma}\cdot\mathbf{n}]_-^+ = 0, \quad \text{(Zero tangential traction)} \end{aligned} \tag{2}$$

where $\boldsymbol{n}$ and $\boldsymbol{t}$ are the unit normal and tangential vectors at the boundaries.

The displacement of incident plane wave with incident angle θ in 1-D layed elastic media can be obtained by Thompson-Haskell matrix method (Thomson, 1950; Haskell, 1990; Zhu and Rivera, 2002; Tong et al., 2014). However, with the presence of acoustic layers, we should solve acoustic equations in the acoustic layers in frequency-wavenumber domain:

$$\begin{aligned} &\rho\omega^2 u_x = ikP; \rho\omega^2 u_z = \partial_z P \\ &P = -\kappa(iku_x + \partial_z u_z) \end{aligned} \tag{3}$$

where P is the pressure and κ is the bulk modulus in the acoustic media, ω and k are the angular frequency and the horizontal wavenumber, respectively. The corresponding propagation matrix can be derived analogously to the elastic case (see Appendix A).

Scattered waves generated by heterogeneity within the study region are modeled using the three-dimensional spectral-element method (SEM) (Komatitsch and Tromp, 1999), which offers a powerful framework for incorporating bathymetric effects, free-surface effects, and multiphysics coupling at material interfaces. However, SEM implementations in widely used packages such as SPECFEM (Peter et al., 2011) typically focus on solving for the acoustic potential χ rather than the pressure field P:

$$\begin{aligned} &\kappa^{-1}\ddot{\chi} = \nabla\cdot\left(\rho^{-1}\nabla\chi\right) \\ &\boldsymbol{u} = \rho^{-1}\nabla\chi; \quad P = -\ddot{\chi} \end{aligned} \tag{4}$$

With the virtual of SEM, we can get the weak form in both (isotropic) elastic and acoustic media as:

$$
\begin{aligned}
&\int_V \kappa^{-1}\ddot{\chi}\phi \,\mathrm{d}V = \int_{\Sigma_a} \phi \boldsymbol{n}\cdot\boldsymbol{u}\,\mathrm{d}\Sigma - \int_V \rho^{-1}\nabla\chi\cdot\nabla\phi \\
&\int_V \rho\ddot{u}_i\phi \,\mathrm{d}V = \int_{\Sigma_a+\Sigma_{FS}} \phi T_i \,\mathrm{d}\Sigma - \int_V \sigma_{ij}u_{i,j}\phi_{,j}\,\mathrm{d}V
\end{aligned}
\tag{5}
$$

where ϕ is the test function, Σ_a represents the exterior boundaries of the model that exclude the free surface, Σ_{FS} is the acoustic-elastic boundary, and T_i denotes the traction on the surface.

To leverage the strengths of both 1-D FK simulations and 3-D SEM, we assume that the heterogeneity within the study region is a perturbation superimposed on the background 1-D model used for simulating the FK plane wave. Appropriate boundary conditions for velocity and traction are applied at the edges of the 3-D domain to ensure consistent coupling between the two methods (Liu et al., 2025). Additionally, the Stacey boundary condition (Clayton and Engquist, 1977) is implemented to absorb artificial reflections of scattered waves at the boundaries:

$$
\begin{aligned}
&\boldsymbol{T}-\boldsymbol{T}^0 = -\rho\alpha\left[\hat{\boldsymbol{n}}\cdot\partial_t(\boldsymbol{u}-\boldsymbol{u}^0)\right]\hat{\boldsymbol{n}} - \rho\beta\left[\hat{\boldsymbol{t}}\cdot\partial_t(\boldsymbol{u}-\boldsymbol{u}^0)\right]\hat{\boldsymbol{t}} \\
&\dot{\chi}-\dot{\chi}^0 = -\alpha\rho\,\boldsymbol{n}\cdot(\boldsymbol{u}-\boldsymbol{u}^0)
\end{aligned}
\tag{6}
$$

where α and β are the propagation speeds of the P-wave and S-wave in the medium, respectively. The quantities $\boldsymbol{u}_0$, T_i^0, and $\dot{\chi}_0$ represent the FK displacement, traction, and acoustic potential derived from the 1-D background model, respectively. The vectors $\hat{\boldsymbol{n}}$ and $\hat{\boldsymbol{t}}$ denote the unit normal and tangential vectors along the boundaries. By applying equation (6) into equation (5) we can obtain the contribution of the surface integral:

$$
\begin{aligned}
\int_{\Sigma_a} \phi T_i \,\mathrm{d}\Sigma &= \int_{\Sigma_a} \phi(T_i - T_i^0 + T_i^0)\,\mathrm{d}\Sigma \\
&= \int_{\Sigma_a} \phi T_i^0\,\mathrm{d}\Sigma - \int_{\Sigma_a} \phi\rho\alpha\left[\hat{\boldsymbol{n}}\cdot\partial_t(\boldsymbol{u}-\boldsymbol{u}^0)\right] n_i\,\mathrm{d}\Sigma \\
&\quad - \int_{\Sigma_a} \phi\rho\beta\left[\hat{\boldsymbol{t}}\cdot\partial_t(\boldsymbol{u}-\boldsymbol{u}^0)\right] t_i\,\mathrm{d}\Sigma \\
\int_{\Sigma_a} \phi\boldsymbol{n}\cdot\boldsymbol{u}\,\mathrm{d}\Sigma &= \int_{\Sigma_a} \phi\boldsymbol{n}\cdot(\boldsymbol{u}-\boldsymbol{u}_0+\boldsymbol{u}^0)\,\mathrm{d}\Sigma \\
&= -\int_{\Sigma_a} \phi\frac{\dot{\chi}-\dot{\chi}^0}{\alpha\rho}\,\mathrm{d}\Sigma + \int_{\Sigma_a} \phi\boldsymbol{n}\cdot\boldsymbol{u}^0\,\mathrm{d}\Sigma
\end{aligned}
\tag{7}
$$

From equation (7), we require the background velocity and traction in the elastic media, as well as the displacement and time derivative of the potential in the acoustic media, to implement the Stacey boundary conditions.

Numerical Examples

Benchmark for a 1-D Model

In this study, we perform a benchmark test to validate the correctness of our method. The model is a 1-D layered model, consisting of a 5-km thick water layer overlying a 1-D isotropic elastic model, as detailed in Table 1. The injected wave is a P-wave characterized by a back azimuth of 68° and a take-off angle of 20° (Figure 1). The source time function is a Gaussian function a dominant frequency of $f_0 = 0.5$ Hz:

TABLE 1.
Model Description

Layer Number	$\rho\ (kg/m^3)$	V_p (m/s)	V_s (m/s)	Thickness (m)
1	1030.	1500.	0.	5000.
2	2720.	5800.	3460.	15000.
3	2920.	6500.	3850.	15000.
4	3423.	8060.	4530.	∞.

$$s(t) = \frac{f_0}{\sqrt{\pi}} e^{-(f_0 t)^2} \tag{8}$$

We compare the results from a hybrid simulation that combines the FK and SEM methods with those obtained from a semi-analytical solution utilizing the FK method alone. The comparison focuses on the final displacement and pressure recorded at two receivers: one positioned within the elastic media and the other located in the water column. Figure 2 illustrates the three-component displacement seismograms recorded by an ocean bottom seismometer (OBS, labeled R_1 in Figure 1). Additionally, the bottom subplot of Figure 2 displays the comparison of pressure. The results from the 3-D SEM-FK hybrid method align closely with those from the FK method, demonstrating a maximum difference of less than 0.8% of the maximum amplitude of the seismograms. Figure 3 presents a comparison of seismograms (X and Z components) recorded at receivers R_1 and R_2 as shown in Figure 1. The Z component is continuous, indicating that the normal displacement remains continuous across the acoustic-elastic boundary. In contrast, the X component is discontinuous, which is tangential to the boundary. This observation confirms the correctness of the simulation.

Full-waveform Inversion for OBS's Receiver Functions

Ocean bottom seismometers (OBS) play a crucial role in oceanic seismology, providing a valuable tool for imaging Earth's interior in regions with sparse seismic receiver coverage. A key technique for investigating subsurface structure beneath OBS deployments is the analysis of receiver functions (RFs). RFs effectively capture signals originating from both seismic discontinuities and subsurface heterogeneity. A significant advantage of RF analysis is that the source wavelet is largely removed by deconvolving the horizontal components with the vertical component. This property enables direct waveform inversion without the need for precise waveform alignment or the estimation of the source time function (Wang et al., 2021).

This study investigates the application of full-waveform inversion (FWI) to teleseismic receiver functions (RFs) recorded by ocean-bottom seismometers (OBS). The synthetic velocity model simulates a subduction zone, where the seafloor is positioned at 3 km with 51 OBS stations deployed directly upon it (Figure 4). The primary feature is a subduction slab, introduced as a ±10% perturbation in both ρ, V_p and V_s) relative to the layered background model (detailed in Table 2), affecting both the oceanic crust and the underlying oceanic mantle . This structure is generally located around 100 km depth (Figure 4).

To generate the 'observed' data, teleseismic responses were simulated for eight distinct back-azimuth angles, chosen to be equidistantly spaced within the range of $0° - 315°$, utilizing this complex subduction model. For comparison, and to serve as a starting model for inversion, P-wave RFs are also computed from simulated seismograms generated using only

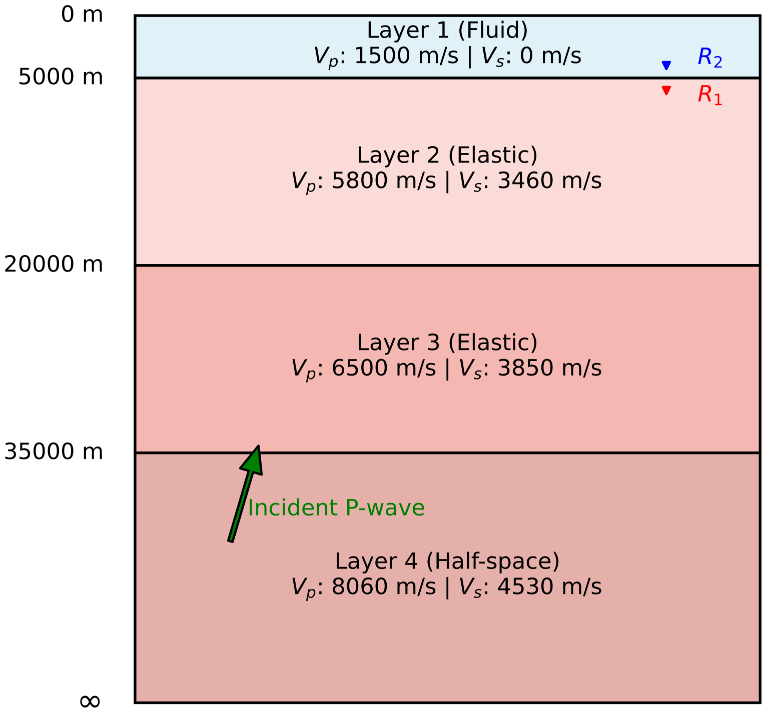

Figure 1. Illustration of the geometry for the 3-D SEM-FK hybrid method. The blue triangles represent the two receivers utilized in the benchmark test, positioned near the acoustic-elastic boundary. Green arrows indicate the propagation direction of the teleseismic plane waves

---

the 1-D background model. The simulated 'observed' seismograms on the radial (R) components are displayed in Figures 5 and 6. Prominent multiples, generated by the velocity anomalies are evident in the radial component seismograms. Receiver functions were subsequently computed employing a time-domain deconvolution method and a Gaussian filter with Gaussian filter parameter $a = 1.5$. Figure 7 (left column) illustrates the resulting receiver functions on event 2 (back azimuth = 45°), displaying prominent arrivals from both the direct P-wave and scattered waves generated by subsurface discontinuities. The observed mismatch between RFs derived from the complex model ('observations') and those from the 1-D background model ('synthetics') primarily arises from the velocity perturbations.

The misfit function used in this example is the L_2 norm of the receiver function difference:

$$\chi = \int_0^T \frac{1}{2}\left[RF(t) - RF^o(t)\right]^2 \,\mathrm{d}t = \int_0^T \frac{1}{2}\Delta R(t)^2 \,\mathrm{d}t \tag{9}$$

we can derive the adjoint sources as (De Jong et al., 2022; Xu et al., 2023):

$$\begin{aligned} f_H^{\dagger}(T-t) &= \Re\,\mathcal{F}^{-1}\left\{\frac{\Delta\hat{R}(\omega)}{\left[Z(\omega)e^{i\omega t_0}\right]^*}\right\}(t) \\ f_Z^{\dagger}(T-t) &= \Re\,\mathcal{F}^{-1}\left\{\frac{\Delta\hat{R}(\omega)\left[H(\omega)e^{i\omega t_0}\right]^*}{\left[\left(Z(\omega)e^{i\omega t_0}\right)^*\right]^2}\right\}(t) \end{aligned} \tag{10}$$

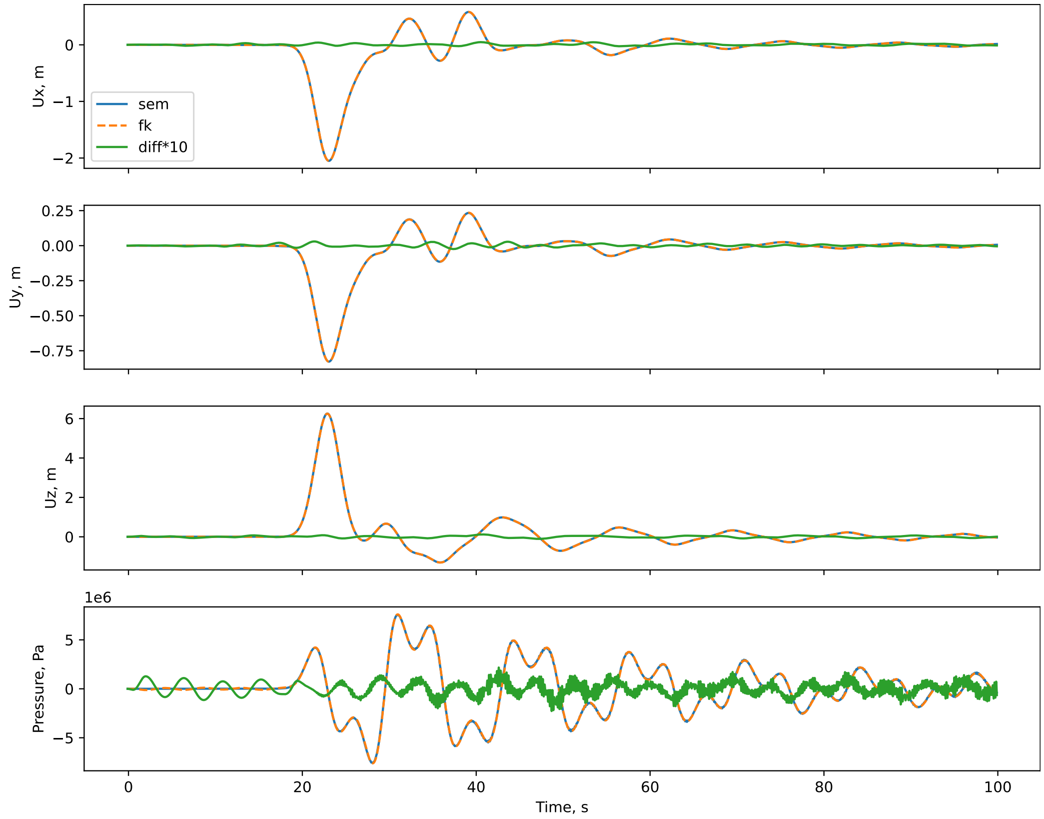

Figure 2. Seismogram benchmark comparing the FK and FK-SEM methods for the 1D layered model. The results are shown for receiver R_1, situated within the elastic medium in immediate proximity to the fluid-solid interface (ocean bottom). From top to bottom, the panels display the x-, y-, and z-components of displacement, followed by the fluid pressure.

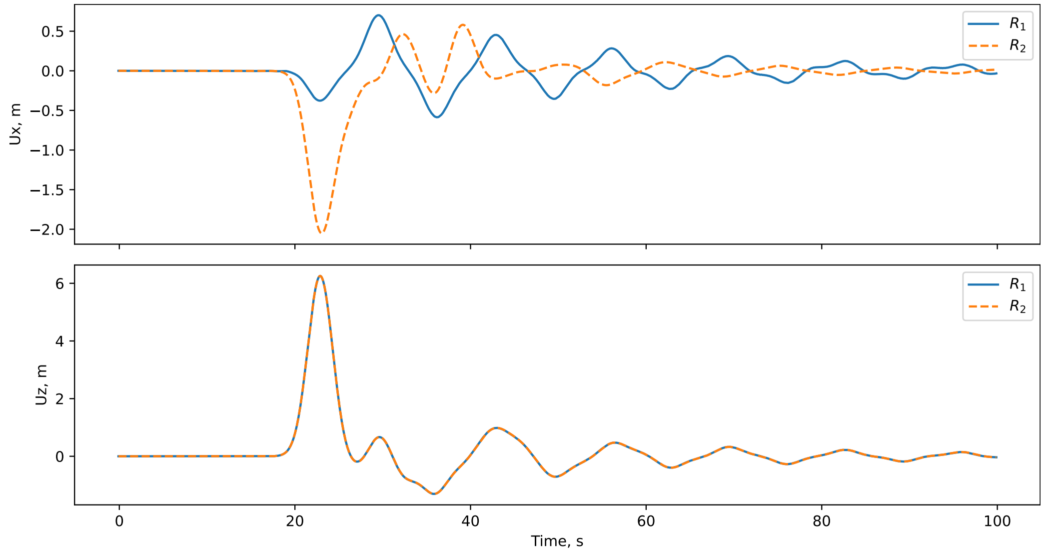

Figure 3. Top: Comparison of tangential displacement components recorded at receivers R_1 (elastic) and R_2 (acoustic). Bottom: Benchmark results for the vertical displacement at receiver R_1, demonstrating the coupling between elastic wave propagation and the pressure field behavior at the fluid-solid interface.

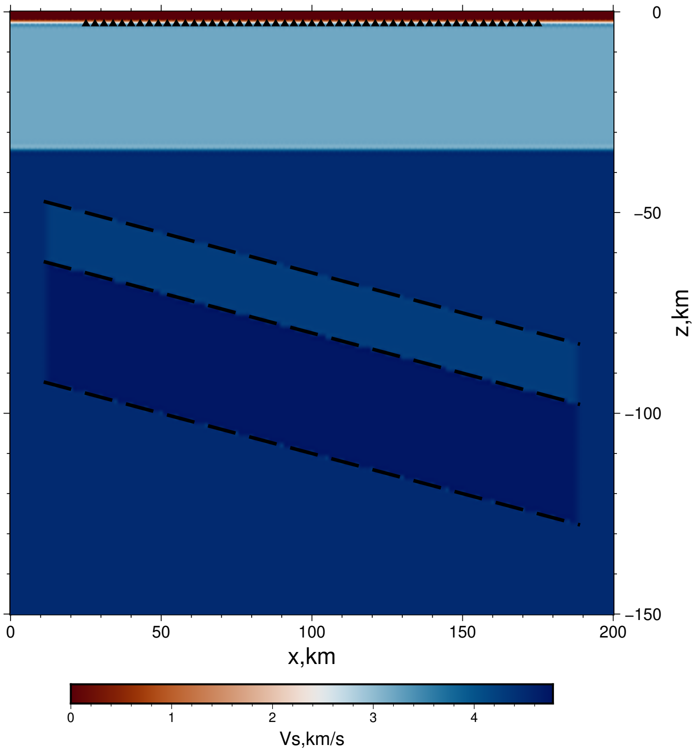

Figure 4. Two-layer subduction zone model used in numerical experiments. The bathymetry is setting at 3km, and the acoustic velocity in the ocean is about 1.5 km/s. The receivers (triangulars) are put directly on the bathymetry. The dashed lines

where $\mathcal{F}^{-1}$ denotes the inverse Fourier transform, $\Re\{\cdot\}$ represents the real part of the result, t_0 is the applied time shift in receiver function analysis, and $\{\}^*$ indicates the complex conjugate. Upon obtaining the gradient of the misfit function with respect to the model parameters, the model is updated using a steepest descent method. The initial step length is set to 2% of the maximum velocity in the starting model. To ensure convergence, the step size is adaptively reduced by 10% if the current misfit exceeds that of the previous iteration. To mitigate strong sensitivity artifacts near the receivers, Gaussian smoothing is applied to regularize the derivatives. During the inversion, material properties in the fluid layer are not updated, as these represent prior information typically well-constrained by oceanographic investigations.

This iterative workflow is applied for 80 iterations, yielding the final inverted model M_{80}, as shown in Figure 9. We observe that the two-layer slab structure has been well recovered through full-waveform inversion. Figures 7 and 8 present a comparison of synthetic and 'observed' receiver functions (RFs) for two of the eight events (additional comparisons are provided in the supplementary materials), displaying results for both the initial model (M_{00}) and the inverted model (M_{80}). The reduction in mismatch between synthetics and 'observations' is evident, particularly for scattered waves originating from the slab. This significant reduction is also quantifiable by an approximate 92% misfit reduction observed in M_{80}. These results confirm the effectiveness of the inversion, highlighting the potential of our method for future investigations of subsurface geodynamics in complex oceanic environments.

TABLE 2. **Background Model for OBS Example**

Layer Number	$\rho\ (kg/m^3)$	V_p (m/s)	V_s (m/s)	Thickness (m)
1	1020	1500	0	3000-5000
2	2600	5800	3200	32000
3	3400	8000	4500	∞

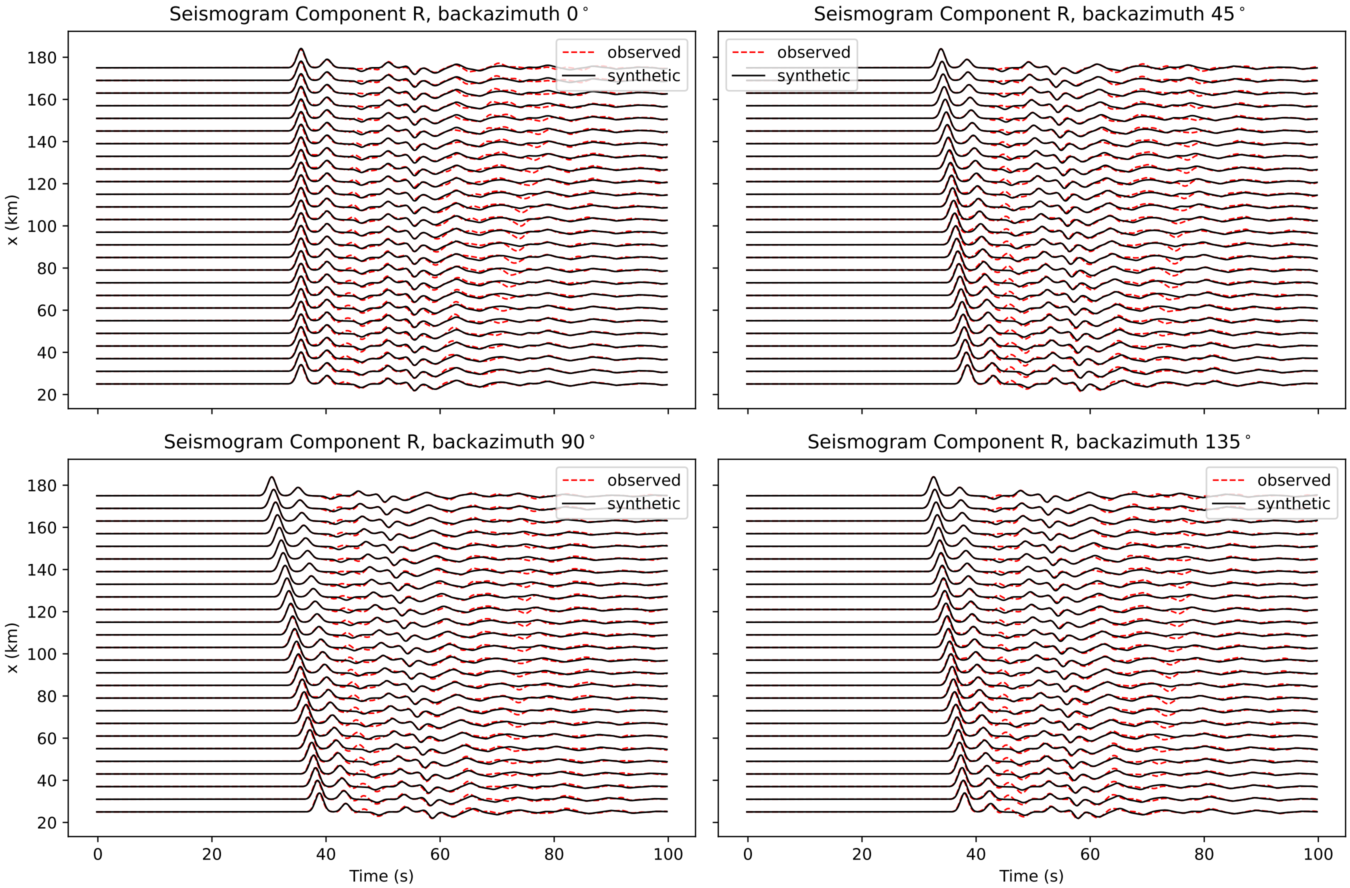

Figure 5. Radial (R) component seismograms for the first four back-azimuth angles. Synthetic data are shown by black solid lines, and 'observed' data by dashed magenta lines. For clarity, seismograms are displayed for only half of the receiver stations.

Discussion

Despite continuous progress in computational capabilities, high-frequency (1 Hz or above) full numerical simulations of teleseismic waves in oceanic environments remain computationally expensive. The hybrid method developed in this study addresses this challenge by providing an efficient and accurate elastic solver for modeling the interactions between plane-wave type teleseismic energy and regional inhomogeneities. Leveraging the spectral element method, our approach seamlessly integrates the effects of inhomogeneities, irregular surfaces, multiphysics coupling (e.g., elastic-acoustic), and adjoint simulations within a general and flexible framework. Our forward and adjoint modeling capabilities are implemented as an extension to the open-source SPECFEM package (Peter et al., 2011). To significantly enhance computational efficiency,

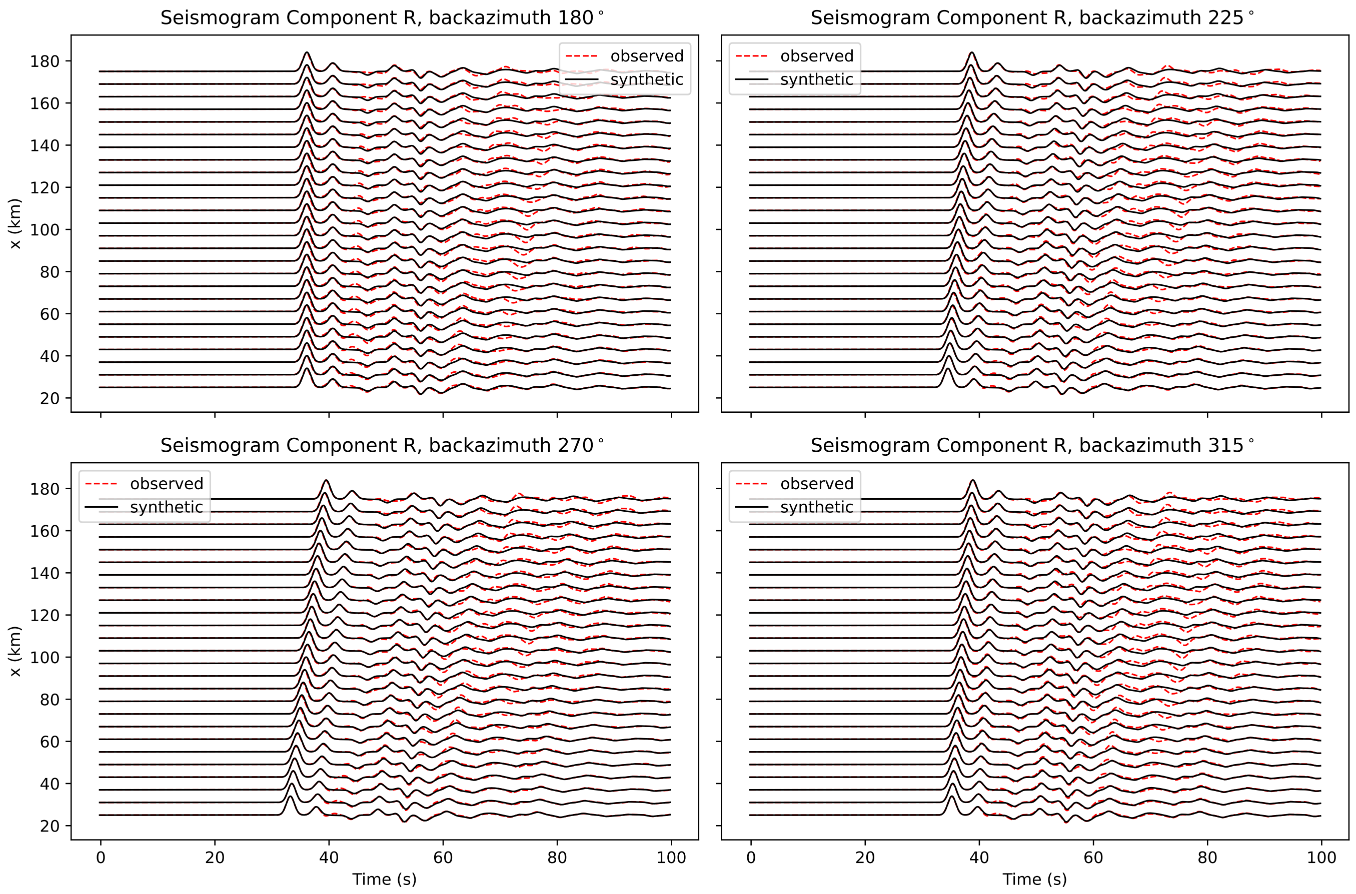

Figure 6. Radial (R) component seismograms for the subsequent four back-azimuth angles. Display format and data representation are identical to Figure 5.

GPU acceleration has been integrated. This optimization yields an approximate five-fold speed-up, enabling forward simulations of the detailed slab model (with approximately 30 million degrees of freedom) up to 2 seconds of physical time to complete in roughly 1 minute on a single NVIDIA H100 card.

It is important to acknowledge certain considerations and limitations of the developed method. This approach employs a one-way coupling scheme, which assumes that inhomogeneities outside the computational study region are negligible or can be accurately approximated by a 1-D model (where external FK field is based on). This assumption may not hold true in all realistic scenarios, particularly in regions with significant external complexities. For such cases, a more advanced coupling approach, such as those based on interface discontinuities (Liu et al., 2025), would need to be extended to fully incorporate acoustic-elastic coupling. Furthermore, the current method is restricted to plane-wave type simulations. While this is well-suited for applications where true amplitude information is not a primary concern (e.g., receiver function analysis), it imposes constraints for other applications. For instance, teleseismic full-waveform imaging directly utilizing all three components would require a pre-processing step to estimate the source time function (Wang et al., 2021) or the use of cross-convolution seismograms (Menke and Levin, 2003) to leverage absolute amplitude information. Finally, application to single-component

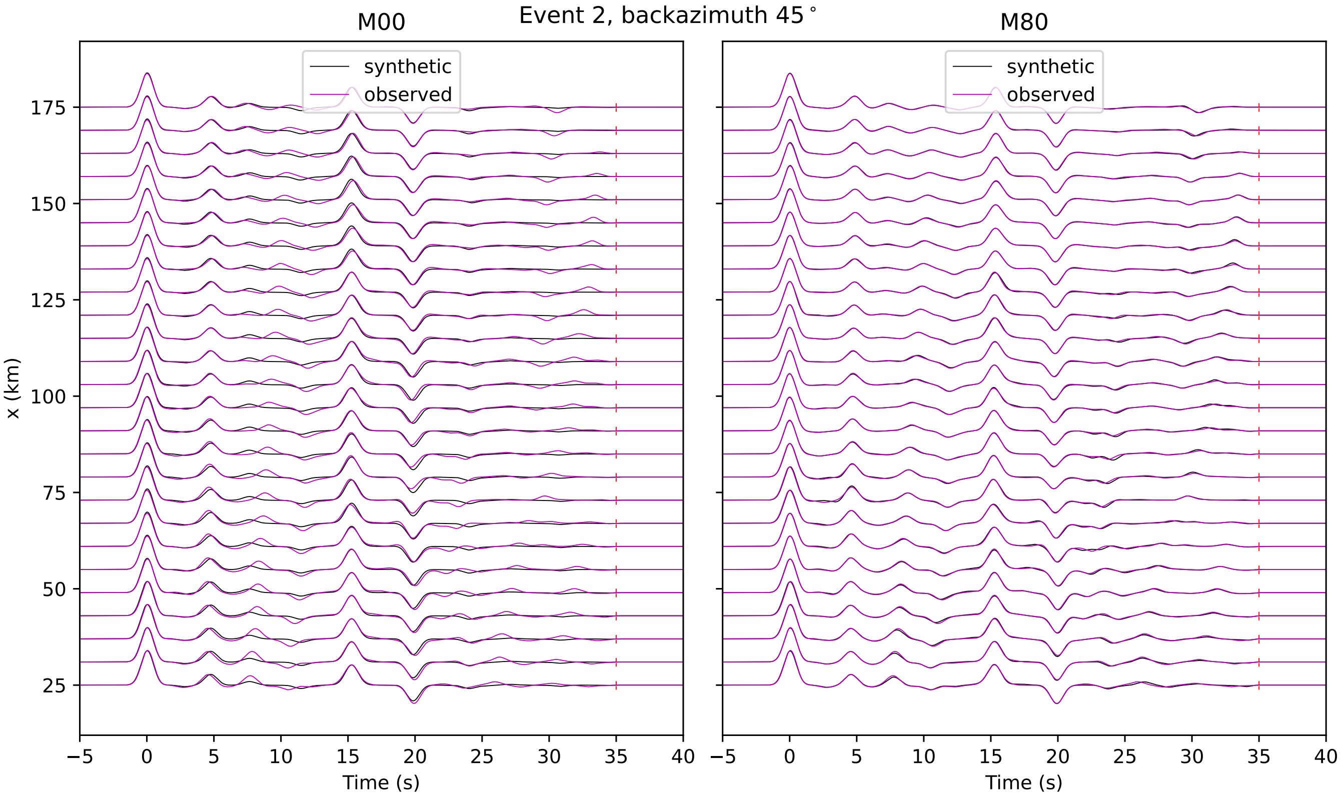

Figure 7. Comparison of Receiver functions for the first M_{00} and the the inverted model (after 80 iterations, M_{80}) for event 2 (back azimuth angle = 45°. The black lines are the observation and the magenta lines are from the synthetic data. The red bars are the time window used in computing misfit functions

receivers (such as MERMAID) presents a limitation, as accurate arrival time estimation is a prerequisite for direct comparison with observed data.

Conclusion

This study presents a novel method for simulating plane-wave-based teleseismic responses in complex oceanic environments. Developed within the framework of the spectral element method, this approach accurately accounts for intricate bathymetric variations and elastic-acoustic coupling during wave propagation. Concurrently, receiver-function-based adjoint methods are being developed to facilitate full-waveform inversion in ocean seismology. To validate the numerical accuracy of our simulation technique, a benchmark test was conducted against 1-D semi-analytical solutions. Furthermore, a synthetic full-waveform inversion OBS experiment was performed on a subduction zone model, demonstrating excellent recovery of subsurface anomalies. In summary, this method offers a robust tool for future geodynamic investigations in oceanic regions, particularly where conventional seismic instrumentation is sparse.

Data and Resources

The computer programs for the implementations of Algorithm 1 in SPECFEM3D_Cartesian has been merged into the SPECFEM3D Github repository (https://github.com/SPECFEM/specfem3d).

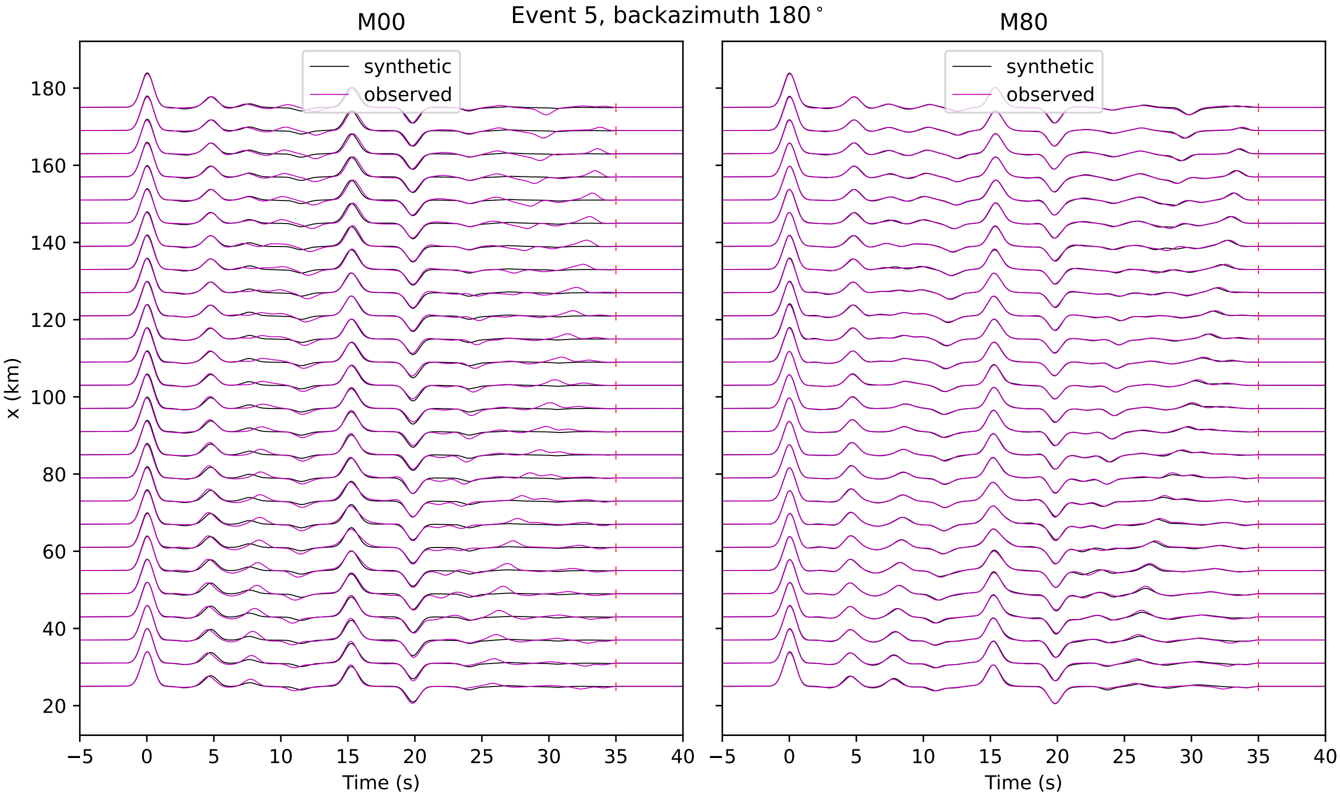

Figure 8. Same as Figure 7, but for event 5

Declaration of Competing Interests

The authors acknowledge that there are no conflicts of interest recorded.[1]

Acknowledgments

The authors acknowledge that open-source visualization software GMT, and Python packages Numpy, SciPy, Matplotlib and Obspy are heavily used to produce the figures in this paper. ND, MX and QL are also partially supported by NSERC Discovery grant #487237. The high-performance computing performed for this research was enabled by support provided by the Digital Research Alliance of Canada (alliance.can.ca).

Appendix A Propagation Matrix

P-SV System

For an isotropic Earth model, seismic wave propagation outside the source region is governed by the homogeneous elastodynamic equation in the frequency domain:

$$-\rho\omega^2 u_i = \left(\lambda u_{k,k}\delta_{ij} + \mu u_{i,j} + \mu u_{j,i}\right)_{,j} \tag{11}$$

---

[1] The authors acknowledge that there are no conflicts of interest recorded.

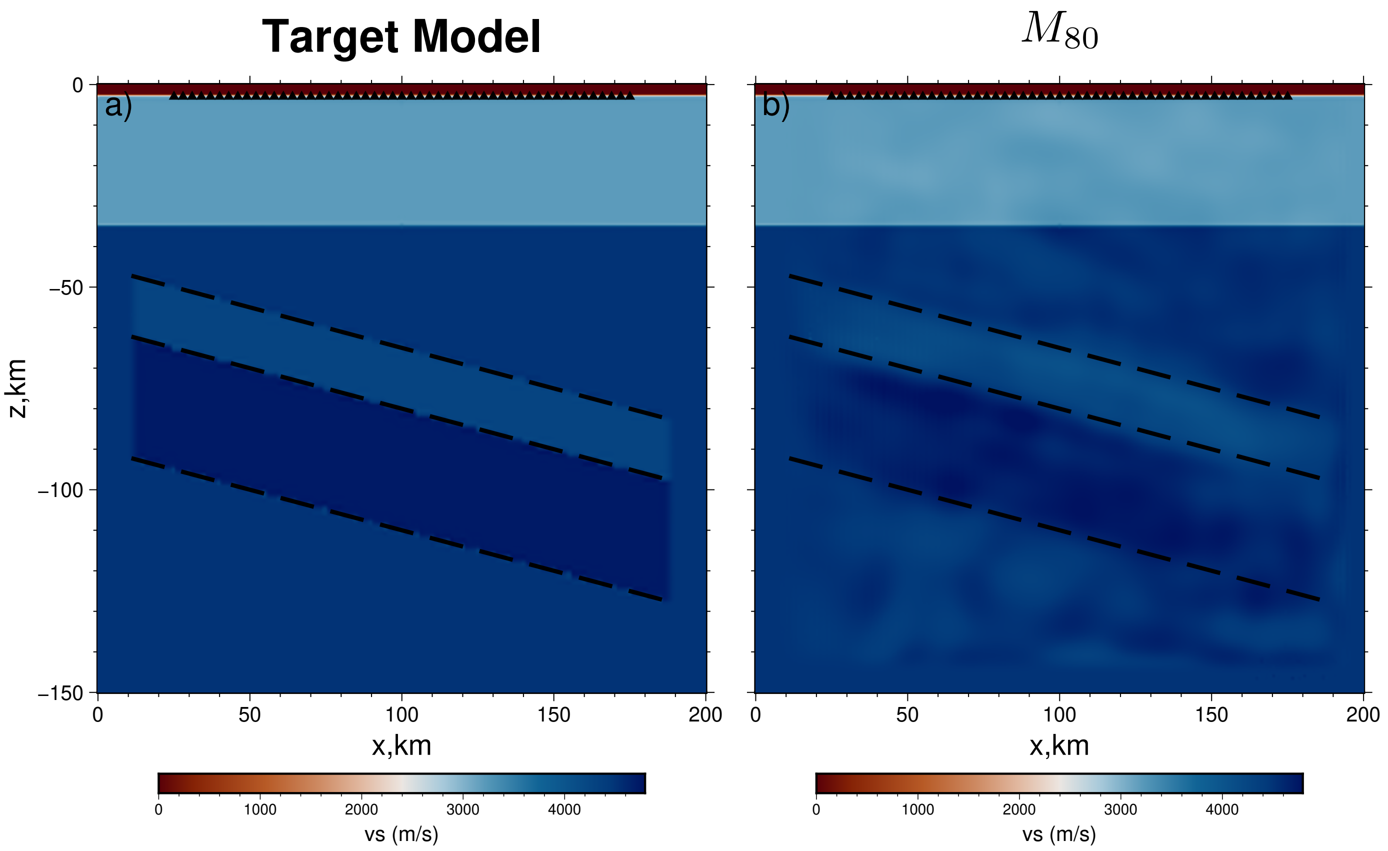

Figure 9. Comparison of true and recovered V_s model (M_{80}) .

For a layered model within the P-SV system, the wave equation can be represented as a first-order system of ordinary differential equations (ODEs) by defining a displacement-traction vector $\boldsymbol{f}$ such that $\boldsymbol{y} = \boldsymbol{f} e^{i(\omega t - kx)}$. This vector satisfies:

$$\frac{\mathrm{d}}{\mathrm{d}z}\boldsymbol{f} = \boldsymbol{A}\boldsymbol{f} \tag{12}$$

where:

$$\boldsymbol{f} = [y_1, y_2, y_3, y_4]^T = [u_x/i, u_z, i\sigma_{xz}, \sigma_{zz}]^T \tag{13}$$

The system matrix $\boldsymbol{A}$ is given by:

$$\boldsymbol{A} = \begin{bmatrix} 0 & -k & \frac{1}{\mu} & 0 \\ (1-2\xi)k & 0 & 0 & \frac{\xi}{\mu} \\ 4k^2\mu(1-\xi) - \rho\omega^2 & 0 & 0 & k(2\xi - 1) \\ 0 & -\rho\omega^2 & k & 0 \end{bmatrix} \tag{14}$$

with the following auxiliary relations:

$$\xi = \frac{\mu}{\lambda + 2\mu}, \quad y_3 = k\mu y_2 + \mu\frac{\mathrm{d}y_1}{\mathrm{d}z}, \quad y_4 = -\lambda k y_1 + (\lambda + 2\mu)\frac{\mathrm{d}y_2}{\mathrm{d}z} \tag{15}$$

We decompose matrix $\boldsymbol{A}$ using its eigenvalues and eigenvectors:

$$\boldsymbol{A} = \boldsymbol{E}\boldsymbol{\Lambda}\boldsymbol{E}^{-1} = \sum_{i=1}^{4} s_i \boldsymbol{r}_i \boldsymbol{l}_i^T \tag{16}$$

where the eigenvalues s_i correspond to the vertical wavenumbers for S and P waves:

$$s_{1,2} = \mp i\nu_s = \mp i\omega\sqrt{\beta^{-2} - p^2}, \quad s_{3,4} = \mp i\nu_p = \mp i\omega\sqrt{\alpha^{-2} - p^2} \tag{17}$$

By expanding $\boldsymbol{f}$ in the basis of the right eigenvectors $\boldsymbol{r}_i$, we obtain a set of decoupled ODEs:

$$\boldsymbol{f} = \sum_{i=1}^{4} c_i \boldsymbol{r}_i \Rightarrow \frac{\mathrm{d}}{\mathrm{d}z} c_i = s_i c_i \tag{18}$$

The general solution is then:

$$\boldsymbol{f}(z) = \sum_{i=1}^{4} w_i e^{s_i z} \boldsymbol{r}_i = \boldsymbol{E}\boldsymbol{\Lambda}(z)\boldsymbol{w} \tag{19}$$

where $\boldsymbol{w}$ represents the amplitudes of the up-going and down-going waves, and $\boldsymbol{\Lambda}(z)$ is the diagonal phase matrix $\Lambda(z)_{jj} = e^{s_j z}$. The matrix $\boldsymbol{E}$, composed of the right eigenvectors, is:

$$\boldsymbol{E} = \begin{bmatrix} -i\nu_s/k & i\nu_s/k & 1 & 1 \\ 1 & 1 & -i\nu_p/k & i\nu_p/k \\ 2k\mu\gamma_1 & 2k\mu\gamma_1 & -2i\mu\nu_p & 2i\mu\nu_p \\ -2i\mu\nu_s & 2i\mu\nu_s & 2k\mu\gamma_1 & 2k\mu\gamma_1 \end{bmatrix} \tag{20}$$

To relate the displacement-traction vector across a layer of thickness $h = z_n - z_{n-1}$, we define $\boldsymbol{f}_n = \boldsymbol{f}(z_n)$. The state at the top and bottom of the n-th layer is related by the propagator matrix $\boldsymbol{P}_n$:

$$\boldsymbol{f}_n = \boldsymbol{E}\boldsymbol{\Lambda}(z_n - z_{n-1})\boldsymbol{E}^{-1}\boldsymbol{f}_{n-1} = \boldsymbol{P}_n \boldsymbol{f}_{n-1} \tag{21}$$

The explicit form of the propagator matrix $\boldsymbol{P}_n$ is provided by (Tong et al., 2014):

$$\boldsymbol{P}_n = \gamma \begin{bmatrix} C_\alpha - \gamma_1 C_\beta & X_\beta - \gamma_1 Y_\alpha & \frac{Y_\alpha - X_\beta}{2k\mu} & \frac{C_\beta - C_\alpha}{2k\mu} \\ X_\alpha - \gamma_1 Y_\beta & C_\beta - \gamma_1 C_\alpha & \frac{C_\alpha - C_\beta}{2k\mu} & \frac{Y_\beta - X_\alpha}{2k\mu} \\ 2k\mu(X_\alpha - \gamma_1^2 Y_\beta) & 2k\mu\gamma_1(C_\beta - C_\alpha) & C_\alpha - \gamma_1 C_\beta & \gamma_1 Y_\beta - X_\alpha \\ 2k\mu\gamma_1(C_\alpha - C_\beta) & 2k\mu(X_\beta - \gamma_1^2 Y_\alpha) & \gamma_1 Y_\alpha - X_\beta & C_\beta - \gamma_1 C_\alpha \end{bmatrix} \tag{22}$$

where the trigonometric terms are defined as:

$$C_{\alpha,\beta} = \cos(\nu_{p,s}h), \quad S_{\alpha,\beta} = -\sin(\nu_{p,s}h), \quad X_{\alpha,\beta} = \frac{-i\nu_{p,s}S_{\alpha,\beta}}{\omega p}, \quad Y_{\alpha,\beta} = \frac{i\omega p S_{\alpha,\beta}}{\nu_{p,s}}$$

By applying Equation (21) recursively and enforcing continuity at each interface, the vector at the free surface $\boldsymbol{f}_n$ is related to the wave field in the half-space $\boldsymbol{w}$ by:

$$\boldsymbol{f}_n = \boldsymbol{P}_n \cdots \boldsymbol{P}_1 \boldsymbol{E}_0 \boldsymbol{w} = \boldsymbol{N}\boldsymbol{w} \tag{23}$$

where $\boldsymbol{f}_n = [y_1, y_2, 0, 0]^T$ at the free surface.

For a P-wave injection, we assume no up-going SV waves in the half-space ($w_1 = 0$) and a unit incident P-wave ($w_3 = 1$). Substituting these into Equation (23) and partitioned for the zero-traction boundary condition:

$$\begin{bmatrix} 0 \\ 0 \end{bmatrix} = \begin{bmatrix} N_{32} & N_{34} \\ N_{42} & N_{44} \end{bmatrix} \begin{bmatrix} w_2 \\ w_4 \end{bmatrix} + \begin{bmatrix} N_{33} \\ N_{43} \end{bmatrix} w_3 \tag{24}$$

The reflected amplitudes w_2 and w_4 are then solved via:

$$\begin{bmatrix} w_2 \\ w_4 \end{bmatrix} = - \begin{bmatrix} N_{32} & N_{34} \\ N_{42} & N_{44} \end{bmatrix}^{-1} \begin{bmatrix} N_{33} \\ N_{43} \end{bmatrix} w_3 \tag{25}$$

A similar procedure is applied for incident SV-waves by setting the appropriate terms in $\boldsymbol{w}$.

Acoustic Media

If a fluid column (e.g., a water layer) overlies the elastic model, the seismic wave propagation within the fluid is governed by the acoustic wave equation. We define the displacement-pressure vector as:

$$\boldsymbol{f} = [u_z, P]^T \tag{26}$$

The depth evolution of this vector is described by the first-order system:

$$\frac{\mathrm{d}}{\mathrm{d}z} \begin{bmatrix} u_z \\ P \end{bmatrix} = \begin{bmatrix} 0 & \frac{k^2}{\rho\omega^2} - \frac{1}{\rho\alpha^2} \\ \rho\omega^2 & 0 \end{bmatrix} \begin{bmatrix} u_z \\ P \end{bmatrix} \tag{27}$$

The corresponding eigenvalues $s_{1,2}$ and the acoustic propagator matrix $\boldsymbol{Q}_n$ for a layer of thickness h are given by:

$$\begin{aligned} s_{1,2} &= \mp i\nu_p = \mp i\omega\sqrt{\alpha_n^{-2} - p^2} = \mp i\omega\eta \\ \boldsymbol{Q}_n &= \begin{bmatrix} \cos(\nu_p h) & -\frac{\nu_p \sin(\nu_p h)}{\rho\omega^2} \\ \frac{\rho\omega^2 \sin(\nu_p h)}{\nu_p} & \cos(\nu_p h) \end{bmatrix} = \begin{bmatrix} \cos(\nu_p h) & -\frac{p\eta \sin(\nu_p h)}{\rho k} \\ \frac{\rho k \sin(\nu_p h)}{p\eta} & \cos(\nu_p h) \end{bmatrix} \end{aligned} \tag{28}$$

At the seafloor (the acoustic-elastic interface) and the free surface, we impose the following boundary conditions:

$$\begin{aligned} &y_3(z_{n-1}) = 0, \quad \text{(zero shear stress at interface)} \\ &P(z_n) = 0, \quad \text{(vanishing pressure at free surface)} \\ &[u_z(z_{n-1})]_-^+ = 0, \quad \text{(continuity of vertical displacement)} \\ &P(z_{n-1}) = -y_4(z_{n-1}), \quad \text{(continuity of normal stress)} \end{aligned} \tag{29}$$

Note: y_3 and y_4 correspond to the elastic displacement-traction components defined in the previous section. We define the global propagator matrix $\boldsymbol{N}$ for the elastic stack as:

$$\boldsymbol{N} = \boldsymbol{P}_{n-1} \cdots \boldsymbol{P}_1 \boldsymbol{E}_0 \tag{30}$$

For an incident P-wave ($w_1 = 0$), the system is solved by:

$$\begin{bmatrix} N_{32} & N_{34} \\ M_1 & M_3 \end{bmatrix} \begin{bmatrix} w_3 \\ w_6 \end{bmatrix} = \begin{bmatrix} -N_{33}w_4 \\ -M_2 w_4 \end{bmatrix} \tag{31}$$

where the auxiliary vector $\boldsymbol{M}$ incorporates the acoustic-elastic coupling:

$$\begin{bmatrix} M_1 & M_2 & M_3 \end{bmatrix} = \begin{bmatrix} Q_{21} & Q_{22} \end{bmatrix} \begin{bmatrix} N_{22} & N_{23} & N_{24} \\ -N_{42} & -N_{43} & -N_{44} \end{bmatrix} \tag{32}$$

Similarly, for an incident SV-wave ($w_4 = 0$):

$$\begin{bmatrix} N_{32} & N_{34} \\ R_2 & R_3 \end{bmatrix} \begin{bmatrix} w_3 \\ w_6 \end{bmatrix} = \begin{bmatrix} N_{31}w_1 \\ -R_1 w_1 \end{bmatrix} \tag{33}$$

where:

$$\begin{bmatrix} R_1 & R_2 & R_3 \end{bmatrix} = \begin{bmatrix} Q_{21} & Q_{22} \end{bmatrix} \begin{bmatrix} N_{21} & N_{22} & N_{24} \\ -N_{41} & -N_{42} & -N_{44} \end{bmatrix} \tag{34}$$

Traction/Pressure

In FK-SEM coupling, we need velocity/traction/pressure at the injection boundary. But the derivations above don't provide the whole stress tensors at each point. So we're going to derive such parameters.

In elastic media:

$$\begin{aligned} \sigma_{zz} &= y_6 \\ \sigma_{xz} &= y_4/i \\ \sigma_{xx} &= k(\lambda + 2\mu)y_1 + k\lambda(1 - 2\xi)y_1 + \lambda\xi/\mu y_6 \\ \sigma_{yy} &= \frac{\lambda}{2(\lambda + \mu)}(\sigma_{xx} + \sigma_{zz}) \end{aligned} \tag{35}$$

In acoustic media:

$$u_x = \frac{-ik}{\rho\omega^2} P \tag{36}$$

Modified Propagation Matrix for Numerical Stability

The standard propagator matrix $\boldsymbol{P}$ and the eigenvector matrix $\boldsymbol{E}$ can be partitioned into 2×2 blocks as follows:

$$\boldsymbol{P} = \begin{bmatrix} \boldsymbol{A} & k^{-1}\boldsymbol{B} \\ k\boldsymbol{C} & \boldsymbol{M} \end{bmatrix}, \quad \boldsymbol{E} = \begin{bmatrix} \boldsymbol{F} & \boldsymbol{G} \\ k\boldsymbol{H} & k\boldsymbol{J} \end{bmatrix} \tag{37}$$

where $\boldsymbol{A}, \boldsymbol{B}, \boldsymbol{C}, \boldsymbol{M}, \boldsymbol{F}, \boldsymbol{G}, \boldsymbol{H}, \boldsymbol{J}$ are 2×2 sub-matrices. In the limit of low frequencies or small horizontal wavenumbers ($\omega \to 0$), the term $k^{-1} = (\omega p)^{-1}$ introduces a singularity due to the zero denominator. To ensure numerical stability, we define modified matrices $\bar{\boldsymbol{P}}$ and $\bar{\boldsymbol{E}}$ that are independent of the k^{-1} scaling:

$$\bar{\boldsymbol{P}} = \begin{bmatrix} \boldsymbol{A} & \boldsymbol{B} \\ \boldsymbol{C} & \boldsymbol{M} \end{bmatrix}, \quad \bar{\boldsymbol{E}} = \begin{bmatrix} \boldsymbol{F} & \boldsymbol{G} \\ \boldsymbol{H} & \boldsymbol{J} \end{bmatrix} \tag{38}$$

The relationship between the original and modified matrices is given by the similarity transformation:

$$\boldsymbol{P} = \boldsymbol{D}\bar{\boldsymbol{P}}\boldsymbol{D}^{-1}, \quad \boldsymbol{E} = \boldsymbol{D}\bar{\boldsymbol{E}} \tag{39}$$

where $\boldsymbol{D}$ is the scaling matrix:

$$\boldsymbol{D} = \begin{bmatrix} \boldsymbol{I}_{2\times2} & \boldsymbol{0} \\ \boldsymbol{0} & k\boldsymbol{I}_{2\times2} \end{bmatrix} \tag{40}$$

By utilizing this transformation, the product of multiple propagator matrices and the final eigenvector matrix can be evaluated without explicit division by k:

$$\begin{aligned} \boldsymbol{P}_n\boldsymbol{P}_{n-1} &= (\boldsymbol{D}\bar{\boldsymbol{P}}_n\boldsymbol{D}^{-1})(\boldsymbol{D}\bar{\boldsymbol{P}}_{n-1}\boldsymbol{D}^{-1}) = \boldsymbol{D}(\bar{\boldsymbol{P}}_n\bar{\boldsymbol{P}}_{n-1})\boldsymbol{D}^{-1} \\ \boldsymbol{P}_n\boldsymbol{E}_0 &= (\boldsymbol{D}\bar{\boldsymbol{P}}_n\boldsymbol{D}^{-1})(\boldsymbol{D}\bar{\boldsymbol{E}}_0) = \boldsymbol{D}(\bar{\boldsymbol{P}}_n\bar{\boldsymbol{E}}_0) \end{aligned} \tag{41}$$

Consequently, the global matrix $\boldsymbol{N}$, which relates the wavefield in the half-space to the surface, is expressed as:

$$\boldsymbol{N} = \boldsymbol{P}_n \cdots \boldsymbol{P}_1\boldsymbol{E}_0 = \boldsymbol{D}(\bar{\boldsymbol{P}}_n \cdots \bar{\boldsymbol{P}}_1\bar{\boldsymbol{E}}_0) = \boldsymbol{D}\bar{\boldsymbol{N}} \tag{42}$$

A similar modification is applied to the acoustic propagator matrix $\boldsymbol{Q}$ in the fluid domain:

$$\boldsymbol{Q} = \begin{bmatrix} a & k^{-1}b \\ kc & a \end{bmatrix}, \quad \bar{\boldsymbol{Q}} = \begin{bmatrix} a & b \\ c & a \end{bmatrix} \tag{43}$$

The wavefield propagation from the seafloor to the free surface can then be performed entirely in the modified domain:

$$\boldsymbol{f}_n = \boldsymbol{Q}\begin{bmatrix} \boldsymbol{N}_2 \\ -\boldsymbol{N}_4 \end{bmatrix}\boldsymbol{w} = \begin{bmatrix} 1 & 0 \\ 0 & k \end{bmatrix}\bar{\boldsymbol{Q}}\begin{bmatrix} \bar{\boldsymbol{N}}_2 \\ -\bar{\boldsymbol{N}}_4 \end{bmatrix}\boldsymbol{w} \tag{44}$$

where $\boldsymbol{N}_2$ and $\boldsymbol{N}_4$ represent the second and fourth row-blocks of $\boldsymbol{N}$, respectively.

References

Aki, K. and P. Richards (2002). *Quantitative Seismology*. University Science Books.

Arai, R., T. Takahashi, S. Kodaira, Y. Kaiho, A. Nakanishi, G. Fujie, Y. Nakamura, Y. Yamamoto, Y. Ishihara, S. Miura, et al. (2016). Structure of the tsunamigenic plate boundary and low-frequency earthquakes in the southern ryukyu trench. *Nature Communications* **7**(1), 12255.

Chen, M., J. Tromp, D. Helmberger, and H. Kanamori (2007). Waveform modeling of the slab beneath japan. *Journal of Geophysical Research: Solid Earth* **112**(B2).

Clayton, R. and B. Engquist (1977). Absorbing boundary conditions for acoustic and elastic wave equations. *Bull. Seismol. Soc. Am.* **67**, 1529–1540.

De Jong, J., H. Paulssen, T. Van Leeuwen, and J. Trampert (2022). Sensitivity kernels for receiver function misfits in a full waveform inversion workflow. *Geophysical Journal International* **230**(2), 1065–1079.

Fernando, B., K. Leng, and T. Nissen-Meyer (2020). Oceanic high-frequency global seismic wave propagation with realistic bathymetry. *Geophysical Journal International* **222**(2), 1178–1194.

Hammond, J. O., R. England, N. Rawlinson, A. Curtis, K. Sigloch, N. Harmon, and B. Baptie (2019). The future of passive seismic acquisition. *Astronomy & Geophysics* **60**(2), 2–37.

Haskell, N. A. (1990). The dispersion of surface waves on multilayered media. *Vincit veritas: A portrait of the life and work of Norman Abraham Haskell, 1905–1970* **30**, 86–103.

Kan, L.-Y., S. Chevrot, and V. Monteiller (2023). Dehydration of the subducting juan de fuca plate and fluid pathways revealed by full waveform inversion of teleseismic p and sh waves in central oregon. *Journal of Geophysical Research: Solid Earth* **128**(4), e2022JB025506.

Komatitsch, D., C. Barnes, and J. Tromp (2000). Simulation of anisotropic wave propagation based upon a spectral element method. *Geophysics* **65**(4), 1251–1260.

Komatitsch, D. and J. Tromp (1999). Introduction to the spectral element method for three-dimensional seismic wave propagation. *Geophysical journal international* **139**(3), 806–822.

Lin, J., S. Fang, R. He, Q. Tang, F. Qu, B. Wang, and W. Xu (2024). Monitoring ocean currents during the passage of typhoon muifa using optical-fiber distributed acoustic sensing. *Nature Communications* **15**(1), 1111.

Liu, T., N. Du, T. Lei, K. Wang, B. He, P. Tong, G. Grasselli, and Q. Liu (2025). Seismic wavefield injection based on interface discontinuity: theory and numerical implementation based upon the spectral-element method. *Geophysical Journal International* **241**(1), 658–673.

Luo, B., W. Trainor-Guitton, E. Bozdağ, L. LaFlame, S. Cole, and M. Karrenbach (2020). Horizontally orthogonal distributed acoustic sensing array for earthquake-and ambient-noise-based multichannel analysis of surface waves. *Geophysical Journal International* **222**(3), 2147–2161.

Lyu, C., Y. Capdeville, and L. Zhao (2020). Efficiency of the spectral element method with very high polynomial degree to solve the elastic wave equation. *Geophysics* **85**(1), T33–T43.

Menke, W. and V. Levin (2003). The cross-convolution method for interpreting sks splitting observations, with application to one and two-layer anisotropic earth models. *Geophysical Journal International* **154**(2), 379–392.

Nissen-Meyer, T., A. Fournier, and F. Dahlen (2008). A 2-d spectral-element method for computing spherical-earth seismograms—ii. waves in solid–fluid media. *Geophysical Journal International* **174**(3), 873–888.

Nolet, G., J. D. Simon, and S. Bonnieux (2024). How accurately are mermaid seismograms located? *Seismological Research Letters* **95**(4), 2368–2374.

Peter, D., D. Komatitsch, Y. Luo, R. Martin, N. Le Goff, E. Casarotti, P. Le Loher, F. Magnoni, Q. Liu, C. Blitz, et al. (2011). Forward and adjoint simulations of seismic wave propagation on fully unstructured hexahedral meshes. *Geophysical Journal International* **186**(2), 721–739.

Pipatprathanporn, S. and F. J. Simons (2022). One year of sound recorded by a mermaid float in the pacific: Hydroacoustic earthquake signals and infrasonic ambient noise. *Geophysical Journal International* **228**(1), 193–212.

Pipatprathanporn, S. and F. J. Simons (2024). Waveform modelling of hydroacoustic teleseismic earthquake records from autonomous mermaid floats. *Geophysical Journal International* **239**(1), 136–154.

Rowe, C. A., F. J. Núñez-Cornú, D. Núñez, S. Bilek, and N. Lindsey (2022). Advances in ocean bottom seismology.

Simon, J. D., F. J. Simons, and J. C. Irving (2021). A mermaid miscellany: Seismoacoustic signals beyond the p wave. *Seismological Society of America* **92**(6), 3657–3667.

Thomson, W. T. (1950). Transmission of elastic waves through a stratified solid medium. *J. Appl. Phys.* **21**, 89–93.

Tong, P., D. Komatitsch, T.-L. Tseng, S.-H. Hung, C.-W. Chen, P. Basini, and Q. Liu (2014). A 3-d spectral-element and frequency-wave number hybrid method for high-resolution seismic array imaging. *Geophysical Research Letters* **41**(20), 7025–7034.

Tong, P., D. Yang, D. Li, and Q. Liu (2017). Time-evolving seismic tomography: The method and its application to the 1989 Loma Prieta and 2014 South Napa earthquake area, California. *Geophys. Res. Lett.* **44**, 3165–3175.

Tromp, J., C. Tape, and Q. Liu (2005). Seismic tomography, adjoint methods, time reversal and banana-doughnut kernels. *Geophys. J. Int.* **160**, 195–216.

Wang, K., Y. Wang, X. Song, P. Tong, Q. Liu, and Y. Yang (2022). Full-waveform inversion of high-frequency teleseismic body waves based on multiple plane-wave incidence: Methods and practical applications. *Bulletin of the Seismological Society of America* **112**(1), 118–132.

Wang, K., Y. Yang, C. Jiang, Y. Wang, P. Tong, T. Liu, and Q. Liu (2021). Adjoint tomography of ambient noise data and teleseismic p waves: Methodology and applications to central california. *Journal of Geophysical Research: Solid Earth* **126**(6), e2021JB021648.

Webb, S. C. and W. C. Crawford (2010). Shallow-water broadband obs seismology. *Bulletin of the Seismological Society of America* **100**(4), 1770–1778.

Wehner, D., N. Rawlinson, T. Greenfield, Daryono, M. S. Miller, P. Supendi, C. Lü, and S. Widiyantoro (2022). Sassier22: Full-waveform tomography of the eastern indonesian region that includes topography, bathymetry, and the fluid ocean. *Geochemistry, Geophysics, Geosystems* **23**(11), e2022GC010563.

Wei, X., Y. Shen, J. Caplan-Auerbach, and J. K. Morgan (2021). An obs array to investigate offshore seismicity during the 2018 kīlauea eruption. *Seismological Society of America* **92**(1), 603–612.

Williams, E. F., M. R. Fernández-Ruiz, R. Magalhaes, R. Vanthillo, Z. Zhan, M. González-Herráez, and H. F. Martins (2021). Scholte wave inversion and passive source imaging with ocean-bottom das. *The Leading Edge* **40**(8), 576–583.

Xu, M., K. Wang, J. Chen, D. Yu, and P. Tong (2023). Receiver function adjoint tomography for three-dimensional high-resolution seismic array imaging: methodology and applications in southeastern tibet. *Geophysical Research Letters* **50**(19), e2023GL104077.

Yamaya, L., K. Mochizuki, T. Akuhara, and K. Nishida (2021). Sedimentary structure derived from multi-mode ambient noise tomography with dense obs network at the japan trench. *Journal of Geophysical Research: Solid Earth* **126**(6), e2021JB021789.

Yang, T., Y. Xu, N. Du, T. Xu, D. Cao, F. Nan, W. Chu, C. Liang, and T. Hao (2023). Gravity inversion constrained by obs receiver function reveals crustal structure in ryukyu trench. *Frontiers in Earth Science* **11**, 1187683.

Zhan, Z. (2020). Distributed acoustic sensing turns fiber-optic cables into sensitive seismic antennas. *Seismological Research Letters* **91**(1), 1–15.

Zhu, H., E. Bozdağ, and J. Tromp (2015). Seismic structure of the european upper mantle based on adjoint tomography. *Geophysical Journal International* **201**(1), 18–52.

Zhu, L. and L. A. Rivera (2002). A note on the dynamic and static displacements from a point source in multilayered media. *Geophysical Journal International* **148**(3), 619–627.

Manuscript Received 05 Month 2026